nature communications

Article

https://doi.org/10.1038/s41467-025-57242-6

Asymmetric rotations slow down diffusion under confinement

Received: 30 November 2024

Accepted: 13 February 2025

Published online: 27 February 2025

Check for updates

Zhiqiang Liu[1,10] ✉, Xun Kan[2,10], Mingbin Gao[3,10], Yi Ji[4], Fangxiu Ye[5], Jingyi Tan[6,7], Fengqing Liu[6,7], Jiamin Yuan[6], Xiaomin Tang[6], Haohan Li[4], Pan Gao[4], Jiaao Xue[1], Qun Cai[1], Naresh C. Osti[8], Niina H. Jalarvo[8], Cheng Li[8], Yongcun Zou[9], Yi Li[9], Shutao Xu[5], Guangjin Hou[4] ✉, Mao Ye[5] ✉, Fujian Liu[2] ✉ & Anmin Zheng[1,6] ✉

Translation and rotation are the two most fundamental forms of diffusion, yet their coupling mechanism is not clear, especially under confinement. Here, we provided evidence of the coupling between rotation and translation using a substituted benzene molecule as an example. A counterintuitive behavior was observed where the movement of the smaller molecule with an asymmetric shape was unexpectedly slower than the larger one with a symmetric shape in confined channels of zeolite. We showed that this diffusion behavior was caused by the presence of the specific and selective interaction of the asymmetric guest with the pores, which increased the local restricted residence time, thus inhibiting the translation under confinement, as further confirmed by dynamic breakthrough curves, uptake measurements, quasi-elastic neutron scattering, and ^{2}H solid-state NMR techniques. Our work correlated asymmetric rotation and diffusion under a confined environment, which enriched our understanding of the coupling between rotation and translation and could shed light on a fundamental understanding of the diffusion process.

Molecules, due to thermal energy, are subject to a continuous irregular movement, referred to as diffusion, in all states of matter[1]. However, confined diffusion in nanoporous materials is intriguing and exhibits many peculiarities compared with that in the condensed phase[2–6]. For example, "single-file diffusion", the restricted motion of interacting particles in narrow micropores with mutual passage exclusion prevalent in many processes, does not obey Fick's laws[7,8]. In contrast to the case in homogeneous media with monotonically decreasing diffusion behavior for various alkane molecules, a phenomenon called "resonant diffusion" was presented where the diffusion coefficient varies periodically with the molecular chain length[9–11]. Notably, diffusion is generally faster at a higher temperature, but our previous work has shown the movement of long-chain molecules slows as the temperature increases under confinement, which is due to the "thermal

[1]Interdisciplinary Institute of NMR and Molecular Sciences, Hubei Province for Coal Conversion and New Carbon Materials, School of Chemistry and Chemical Engineering, Wuhan University of Science and Technology, Wuhan, PR China. [2]National Engineering Research Center of Chemical Fertilizer Catalyst (NERC-CFC), College of Chemical Engineering, Fuzhou University, Fuzhou, PR China. [3]State Key Laboratory of Physical Chemistry of Solid Surfaces, College of Chemistry and Chemical Engineering, Xiamen University, Xiamen, PR China. [4]State Key Laboratory of Catalysis, Dalian National Laboratory for Clean Energy, 2011-Collaborative Innovation Center of Chemistry for Energy Materials, Dalian Institute of Chemical Physics, Chinese Academy of Sciences, Dalian, PR China. [5]National Engineering Research Center of Lower-Carbon Catalysis Technology, iChEM (Collaborative Innovation Center of Chemistry for Energy Materials), Dalian Institute of Chemical Physics, Chinese Academy of Sciences, Dalian, PR China. [6]State Key Laboratory of Magnetic Resonance Spectroscopy and Imaging, Innovation Academy for Precision Measurement Science and Technology, Chinese Academy of Sciences, Wuhan, PR China. [7]University of Chinese Academy of Sciences, Beijing, PR China. [8]Neutron Scattering Division, Oak Ridge National Laboratory, Oak Ridge, TN, USA. [9]State Key Laboratory of Inorganic Synthesis and Preparative Chemistry, College of Chemistry, Jilin University, Qianjin Street 2699, Changchun, PR China. [10]These authors contributed equally: Zhiqiang Liu, Xun Kan, Mingbin Gao ✉e-mail: zqliu_wh@wust.edu.cn; ghou@dicp.ac.cn; maoye@dicp.ac.cn; fjliu@fzu.edu.cn; zhenganm@wipm.ac.cn

resistance effect"[12]. Kolokathis et al. studied the diffusion of aromatics in silicalite-1 by quasi-elastic neutron scattering (QENS) and molecular dynamics simulations; they found that the *p*-xylene diffused faster than benzene due to lower entropic barriers[13]. Other interesting effects, including the "levitation effect"[14–19], "incommensurate diffusion"[20], "window effect"[21,22], and "trapdoor effect"[23–26] have also been found inside the confined space. It is worth noting that only some of the phenomena mentioned above have been experimentally confirmed (Supplementary Table 1).

Transportation of adsorbates in confined channels is controlled by the interplay between adsorbent–adsorbate and adsorbate–adsorbate interactions, and thus molecular diffusion through pores occurs via different mechanisms[6,27–32]. Normally, diffusion is generally slower for larger molecules due to their stronger adsorption energy. For instance, Gao et al. measured the diffusion coefficients of different alkane species in DNL-6 zeolite by pulsed field gradient NMR (PFG-NMR) and found that they followed the order of $CH_4 > C_2H_6 > C_3H_8$[28]. Jobic et al. showed that diffusion of branched alkanes (a bulkier molecule) was much slower than the one of linear alkanes (smaller molecule) in ZSM-5 by QENS[33]. Van Baten and Krishan showed branched isomers of hexane had lower self-diffusivity than n-hexane[34], and Schuring et al. reported that the self-diffusion coefficient of n-hexane was higher than 2-methylpentane[35]. Verploegh et al. predicted the diffusivities of 30 small molecules in various metal-organic frameworks and found that self-diffusivities decreased with the molecular sizes[36]. DeLuca and other groups predicted the diffusion by adsorption energy, adsorption entropies, and diffusion barriers, which indicated that diffusion was slower for larger molecules in a stronger confined system[29,37–39]. Overall, it was suggested that the diffusion was faster for molecules with small size under a less confined environment.

Symmetry pervades our lives[40], which also strongly affects diffusion, especially in the confined environment. For the MOF materials, it was illustrated that the introduction of asymmetry in the pore blocking the diffusion of tetrahedral methane while allowing linear nitrogen to permeate in the process of nitrogen removal from nature gas[41]. Sharma et al. showed that "levitation effect" (fast diffusion) could only take place for symmetric molecules under confinement[42]. Several groups tried to recover asymmetric diffusion. For example, Shaw et al. claimed asymmetric diffusion mainly came from an asymmetry in the geometry of the pores[43], while Kolomeisky et al. suggested that the interaction potential asymmetry strongly controlled the diffusion[44]. Other explain to asymmetric diffusion by the fact of the molecular shape, charge asymmetry, and asymmetric jump[45–49]. Although asymmetric diffusion has been extensively studied, however, the fundamental understanding and quantitative description of molecular asymmetric diffusion under confinement, as well as experimental verifications were still missing.

Zeolites are ideal microporous materials for studying the confinement effect because the channels and pores of these crystalline structures have precise dimensions[50–52]. In this work, the anomalous behavior in diffusion for varied dihalobenzene molecules in zeolites was observed, where the traditional view that the diffusion coefficient is related to the molecular size and molecular weight has been broken, where a smaller molecule with weaker adsorption moved slower than a larger one with stronger adsorption under confinement. The effect of molecule species, the framework, the temperature and loading on diffusion have also been considered, which clearly illustrates the robust to asymmetric rotations slow diffusion under confinement. In addition, several types of experiments were performed to determine molecular diffusion property. The results provide insights into the mechanism of diffusion slowed by asymmetric rotations inside confined systems.

Results

First, the diffusion behaviors of molecules in the bulk phase were studied, and the self-diffusion coefficient (D_s) was used to quantitatively describe the movement of guest molecules[6]. The initial structure of various m-dihalobenzenes ($C_6H_4F_2$, C_6H_4BrF, and $C_6H_4Br_2$) in the bulk phase is depicted in Fig. 1A and Supplementary Fig. 1 and the parameter sets are listed in Supplementary Table 2. It shows that both the density (Supplementary Table 3) and the molecule size (Supplementary Figs. 2 and 3) follow the order of $C_6H_4F_2 < C_6H_4BrF < C_6H_4Br_2$. The D_s were quantitatively determined based on molecular dynamics (MD) simulations and the slope of the mean square displacement (Supplementary Fig. 1) values, which were 2.21×10^{-9}, 1.35×10^{-9}, and 0.74×10^{-9} m^2/s for $C_6H_4F_2$, C_6H_4BrF, and $C_6H_4Br_2$, respectively (Fig. 1D). Then, we performed pulsed field gradient (PFG) NMR (Supplementary Methods) to investigate the diffusion behavior for three molecules in the bulk phase at 298 K. The echo-attenuation from ^1H PFG NMR followed a mono-exponential decay model well (Fig. 1B), and the self-diffusion coefficients of three substituted benzene molecules were observed in the following order: $C_6H_4F_2$ (3.56×10^{-9} m^2/s) > C_6H_4BrF (1.80×10^{-9} m^2/s) > $C_6H_4Br_2$ (0.75×10^{-9} m^2/s) (Fig. 1E). The simulated self-diffusion coefficients agree reasonably well with results from PFG NMR, which suggest that the diffusion was strongly related to the size and weight of molecules. In particular, the diffusion was slower for larger molecules in the bulk phase.

Next, we turned our attention to the diffusion behaviors of these molecules in zeolite with AFI topology (pore size is 7.3 ×7.3 $Å^2$, Supplementary Fig. 4) under confinement (Fig. 1C and Supplementary Fig. 5). The diffusion order differed for dihalobenzene molecules in the bulk phase. As shown in Fig. 1F, the D_s are 1.25×10^{-8}, 0.93×10^{-8}, and 1.14×10^{-8} m^2/s for $C_6H_4F_2$, C_6H_4BrF, and $C_6H_4Br_2$, respectively, which are inconsistent with the molecular size and adsorption energy (Supplementary Fig. 6). For example, the D_s of $C_6H_4Br_2$ molecule with a bulkier size and stronger interaction (−19.5 kcal/mol) is relatively larger than that of C_6H_4BrF with smaller size and less interaction (−18.6 kcal/mol). This was a counterintuitive diffusion behavior, and the diffusion mechanism could not be uncovered by adsorption energy[38].

To understand the above-mentioned phenomena of different trends of diffusion for dihalobenzene molecules in the bulk phase and inside zeolite, the diffusion trajectories, which can give quantitative information on molecular motion, were obtained[28,53,54]. Figure 2A–C shows the trajectory of center-of-mass (COM) for various representative molecules along the channel of AFI (direction [001]) zeolite. It clearly shows that $C_6H_4F_2$ molecular trajectory is the longest, followed by $C_6H_4Br_2$ and C_6H_4BrF (statistical results are shown in Table 1). These results agree with the order of D_s, further indicating that the diffusion trajectories can be used to analyze the diffusion behaviors[28]. Specifically, the maximum diffusion distances for molecules are mainly due to the significant successive jump in the same direction (Supplementary Fig. 7)[49,55], such as the jump with long distance for $C_6H_4F_2$ during 645–655 ps (Fig. 2A, D), as well as for $C_6H_4Br_2$ during the 515–525 ps (Fig. 2C, F). However, few notable jumps are detected for C_6H_4BrF molecules; they preferred the back and forth motion (Fig. 2B), which corresponds to the slowest diffusion. In addition, in contrast to the forward rotational motion of $C_6H_4F_2$ and $C_6H_4Br_2$, a marked local rotation with less translation is found for C_6H_4BrF (e.g. 445–455 ps in Fig. 2B, E). These results indicate a large jump of $C_6H_4F_2$ and $C_6H_4Br_2$ (Fig. 2D, F) may boost transport, while local dwellings combined with rotation (Fig. 2E) of C_6H_4BrF hinder diffusion.

To evaluate the different rotation behaviors for dihalobenzene molecules, three-dimension (3D) normalized rotational trajectories[56,57] for the C–F ($\vec{\upsilon}_{CF}$) and C–Br ($\vec{\upsilon}_{CBr}$) bonds were obtained. Figure 2G–I shows that the rotational trajectories are symmetric for two $\vec{\upsilon}_{CF}$ and $\vec{\upsilon}_{CBr}$ vectors of $C_6H_4F_2$ (Fig. 2G and Supplementary Fig. 8A) and $C_6H_4Br_2$ (Fig. 2I and Supplementary Fig. 8C) with symmetry. In addition, due to the short C–F bond, $C_6H_4F_2$ can rotate freely with a wide range of rotational trajectories (Fig. 2G), whereas $C_6H_4Br_2$ can only swing along the direction Z because two long C–Br bonds (Fig. 2I and Supplementary Fig. 8C) inhibit rotation. However, there was no symmetry for C_6H_4BrF transport, along with a local swinging motion of the C–Br bond as well as more free rotation of the C–F bond (Fig. 2H and

https://doi.org/10.1038/s41467-025-57242-6

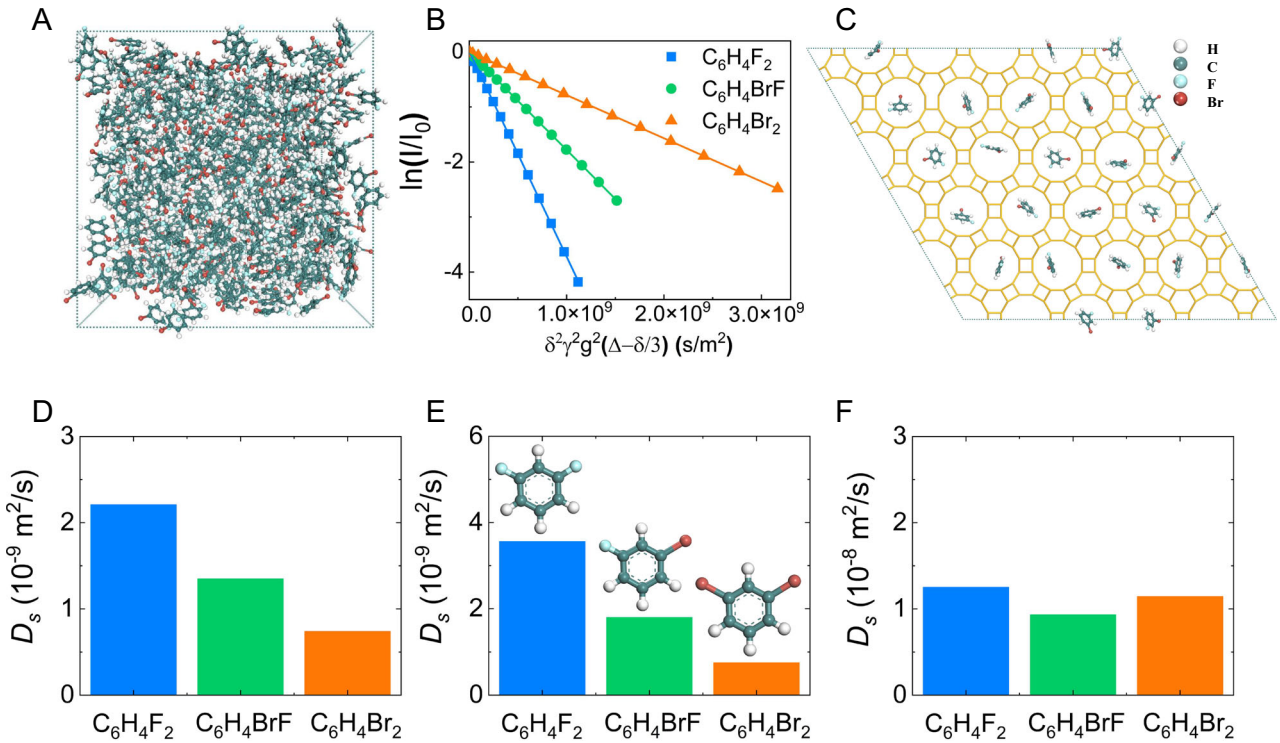

Fig. 1 | Diffusion in the bulk phase and inside zeolite. A Initial structures of C_6H_4BrF (1-bromo-3-fluorobenzene) in the bulk phase. **B** The spin echo-attenuation of PFG NMR as a function of $\delta^2\gamma^2g^2(\Delta-\delta/3)$ on the log-linear scale for $C_6H_4F_2$, C_6H_4BrF and $C_6H_4Br_2$ in the bulk phase. I and I_0 are the signal amplitudes with and without gradient strength (g), γ is the gyromagnetic ratio of the ^1H nucleus, δ is the effective gradient pulse duration, Δ is the diffusion time. **C** Initial structures of C_6H_4BrF inside AFI zeolite. The dark green, white, cyan and dark red balls represent C, H, F and Br atoms, respectively; yellow represents zeolite framework. Self-diffusion coefficient (D_s) for various molecules in the bulk phase by **D** MD simulation and **E** PFG-NMR technique. **F** D_s for various molecules inside AFI zeolite by MD simulation at 298 K.

Supplementary Fig. 8B). Overall, it seems that asymmetric rotation can affect diffusion.

Based on the diffusion trajectory profiles (Fig. 2A–C and Supplementary Fig. 7), the diffusion process can be regarded as a jump-like diffusion, which was directly determined by residence time and jump length between two neighboring basins or cages (Supplementary Fig. 9)[28,58,59]. Table 1 shows the diffusion radius (R) for various molecules in AFI during the diffusion time of 10 ns. Apparently, R follows the order of $C_6H_4F_2$ (141.6 Å) > $C_6H_4Br_2$ (136.1 Å) > C_6H_4BrF (118.1 Å), which is consistent with the order of D_s. Our previous work has shown a continuous-time random-walk (CTRW) coarse graining method can quantitatively investigate the diffusion process by residence time and jump length[28,60]. Generally, shorter residence time (t) in one basin and longer jump length (d) between two consecutive basins lead to fast diffusion with a longer diffusion radius. As presented in Table 1, the jump length is almost the same, indicating that d is not the main factor for the diffusion differences. Fortunately, the residence time is 62.4, 91.8 and 70.5 ps for $C_6H_4F_2$, C_6H_4BrF, and $C_6H_4Br_2$, respectively, which is inverse to the order of D_s, indicating the increased local residence time slowed the diffusion. However, it should be noted that, due to the lack of correlation between rotation and translation, we could not yet reveal the microscopic mechanism of the slowest translation of C_6H_4BrF with the longest residence time.

Several investigations have been done to evaluate the diffusion behaviors from both translation and rotation, which indicated that the interaction between guest and host was important to uncover the diffusion mechanism[13,61–63]. The reduced density gradient (RDG) visualization of the iso-surfaces method (Supplementary Methods) was employed to study the interaction between the guest and host (Fig. 3A–C). It shows that the interaction between zeolite and Br atoms (Fig. 3B, C) is much stronger (the large green region representing van der Waals interaction) than that with F atoms (Fig. 3A, B), and thus the anomalous behavior in diffusion is caused by the presence of the specific and selective interaction of the asymmetric guest with the pores. Here, because C_6H_4BrF is an asymmetric molecule but $C_6H_4Br_2$ and $C_6H_4F_2$ possess symmetry, we tried to correlate the asymmetric rotation and translation. First, the 2D contour plots of probability distribution[49] between the rotational angle difference ($\Delta\theta$) and translation displacement (ΔX) at a time interval of 100 ps are shown in Supplementary Fig. 10. We found that $\Delta\theta$ from two halogen atoms is mainly in the region of −90° to 90° for $C_6H_4F_2$, as well as −60° to 60° for $C_6H_4Br_2$, indicating a symmetric rotation for symmetric molecules. However, the region of rotational angle difference was different ($-90° < \Delta\theta < 30°$), demonstrating that some parts of rotation seriously deviated from symmetry because the C–F bond rotated faster than the C–Br bond for C_6H_4BrF. Regardless of the shape of the molecules, the position with the largest translation distance corresponded to the case where the rotation angle difference was zero, indicating marked jumps were present when the angular rotations were symmetrical.

Furthermore, to evaluate the hindered diffusion behaviors of probe molecules, the 2D free energy contour plots, which can detect simultaneous rotation and translation, were performed. As listed in Fig. 3D–F, the lowest free energy less than 8 K_bT is presented in the region (blue color) where both the rotational angle and translational motion are small, suggesting that molecules are strongly bound in the channel under confinement. In addition, the movement area follows the order of $C_6H_4F_2$, C_6H_4BrF, and $C_6H_4Br_2$, which is the same as the order of molecular size. Specifically, on the iso-free-energy surface (e.g. 9 K_bT), the larger the asymmetric rotation ($\Delta\theta$), the shorter the translational distance (ΔX). Other 2D free energy correlated rotation and translation at different time intervals are shown in Supplementary Fig. 11; these results suggest asymmetric rotations slowed the

https://doi.org/10.1038/s41467-025-57242-6

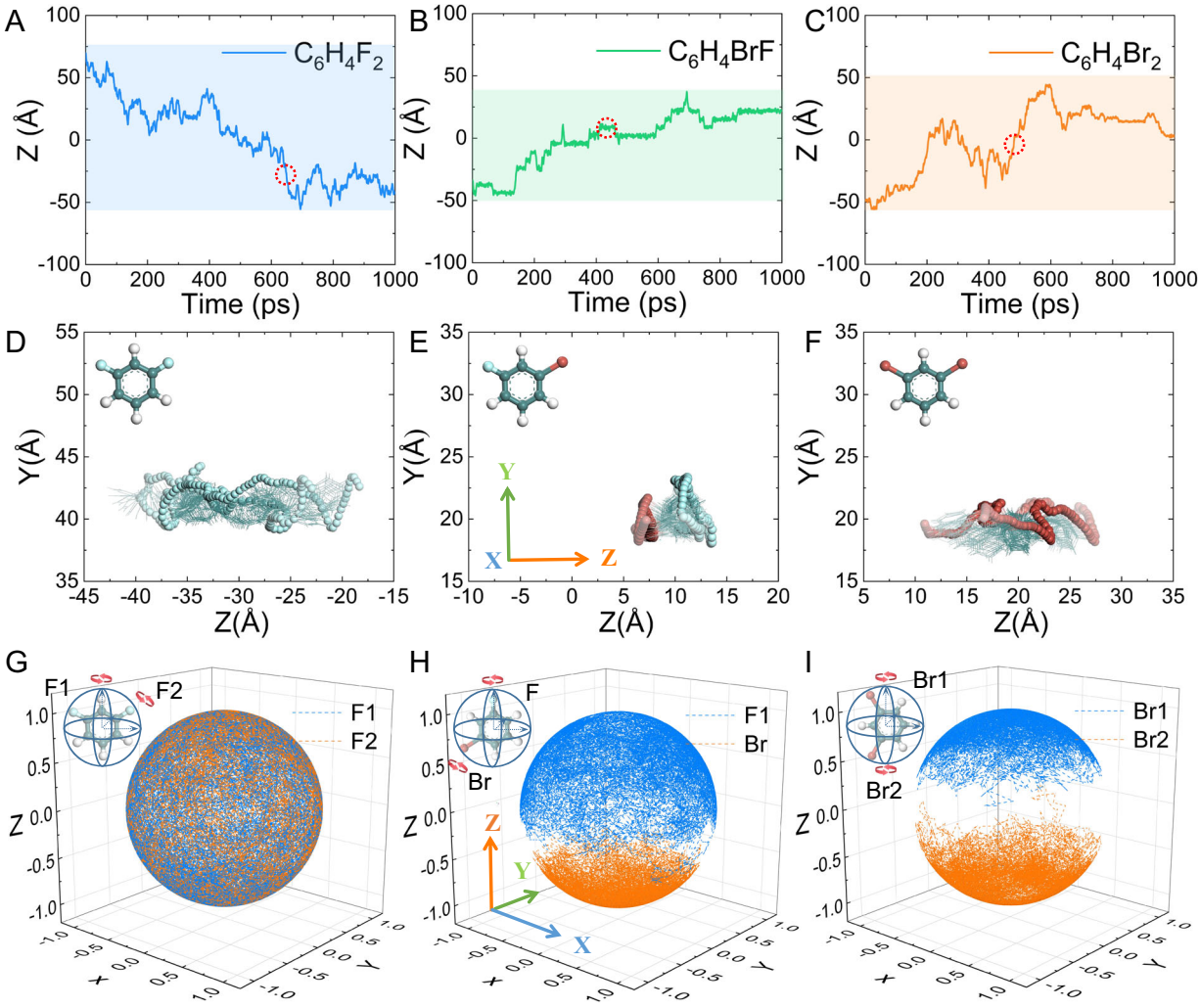

Fig. 2 | Trajectories inside AFI zeolite. Trajectory of center-of-mass for one representative **A** $C_6H_4F_2$, **B** C_6H_4BrF, and **C** $C_6H_4Br_2$ in AFI zeolite along the direction [001] (Z) for 1000 ps. Diffusion process for **D** $C_6H_4F_2$, **E** C_6H_4BrF, and **F** $C_6H_4Br_2$ along the direction [001] for 10 ps. Three-dimensional trajectory of normalized C–F and C–Br bond vector for **G** $C_6H_4F_2$, **H** C_6H_4BrF, and **I** $C_6H_4Br_2$ in AFI zeolite. The dark green, white, cyan and dark red balls represent C, H, F and Br atoms, respectively.

translation in AFI zeolite. Figure 3D, F shows that there are asymmetric rotations ($\Delta\theta \neq 0$) even for symmetric molecules under confinement. And thus, due to the channel of AFI zeolite restricts the asymmetric rotation of $C_6H_4Br_2$ molecules, the diffusion coefficient for $C_6H_4Br_2$ is larger than that for C_6H_4BrF.

The diffusion behaviors of molecules inside the confined channel are strongly correlated with the framework of the zeolite, temperature, loading and molecule species[6,30,31,64]. Both the mesoporous SBA-15 model and microporous zeolites with VFI and MAZ topologies were chosen to investigate the effect of channel dimension on diffusion under confinement. The topologies and initial structure of molecules are shown in Supplementary Figs. 12–14. All the porous materials possess one-dimensional circular channels with the pore size of 20×20, 12.7×12.7, and 7.4×7.4 Å^2 for the SBA-15 model, VFI and, MAZ zeolites, respectively (Supplementary Fig. 4). As shown in Fig. 4A, the diffusion characters are similar for porous materials with a large pore size (i.e. mesoporous SBA-15 model and VFI zeolite), and the D_s follows the order of $C_6H_4F_2 > C_6H_4BrF > C_6H_4Br_2$, which is inversely proportional to the adsorption energy (Supplementary Fig. 15) and residence time (Fig. 4B, C, Supplementary Tables 4 and 5). However, as the pore size decreases to sub-nanometer (e.g. MAZ), the order of diffusion changes. As listed in Fig. 4D and Supplementary Table 6, the D_s is 1.32×10^{-8} m^2/s for $C_6H_4Br_2$, which is larger than C_6H_4BrF (0.76×10^{-8} m^2/s) and consistent with the diffusion order in AFI. It is worth noting that, due to the pore roughness and tortuosity factors of SBA-15 model (Supplementary Fig. 12), the self-diffusion coefficient is comparable with AFI and MAZ zeolites. As indicated by the above two different diffusion orders, confinement affected the diffusion. In the tightly confined space, asymmetric rotations increased the residence time and disrupted the order of molecular diffusion.

In addition, we also considered the effect of concentration (loading), temperature, molecule species and shape of the pore size. As shown in Supplementary Fig. 16A and Table 7, due to the more frequent collision hindering the movement, all the diffusion coefficients decrease as the loading increases in AFI zeolite. Thus, the effect of asymmetric rotations was more pronounced at low loading. Besides loading, the diffusion behavior in AFI at different temperatures was analyzed. We found that the effect of asymmetric rotations decreases as the temperature increases (Supplementary Fig. 16B and Table 8). For example, the D_s is 1.81×10^{-8} and 1.94×10^{-8} m^2/s for C_6H_4BrF and $C_6H_4Br_2$ at 473 K, whereas it reaches 2.96×10^{-8} (C_6H_4BrF) and 3.11×10^{-8} m^2/s ($C_6H_4Br_2$) at 673 K, which may be caused by the higher temperature increases the momentum of molecules and by weakening the contribution of rotation. Overall, higher loading and temperature reduced the contribution of asymmetric rotation during the diffusion process. We also consider the effect of other molecules such as m-

xylene, m-bromotoluene, and m-dibromobenzene (Supplementary Fig. 17) as well as m-difluoropyridine, m-fluorobromopyridine, and m-dibromopyridine (Supplementary Fig. 18), the diffusion anomalous dependence on sorbate size is also present. However, this effect is not fully universal, especially for some large molecules (e.g. 1,2,4-trifluorobenzene, 1,3,5-trifluorobenzene, 1,3-difluoro-5-bromobenzene, 1,3-dibromo-5-fluorobenzene, 1,2,4-tribromobenzene and 1,3,5-tribromobenzene) (Supplementary Fig. 19). Fortunately, as for the elliptical pore size of MOR (6.5 × 7.0 Å^2), the D_s is 2.02×10^{-8}, 0.97×10^{-8} and 1.34×10^{-8} m^2/s for $C_6H_4F_2$, C_6H_4BrF and $C_6H_4Br_2$, respectively. The flexibility of the framework has been considered. The diffusion coefficient of $C_6H_4F_2$, C_6H_4BrF and $C_6H_4Br_2$ in flexible AFI zeolite is 1.12×10^{-8}, 0.82×10^{-8} and 1.11×10^{-8} m^2/s, respectively. Overall, it clearly illustrates the robust degree to which asymmetric rotations slow diffusion under confinement.

Table 1 | Diffusion parameters

Molecule	Diffusivity D_s (×10^{-8} m^2/s)	Diffusion Radius R (Å)	Residence Time t (ps)	Jump Length d (Å)
$C_6H_4F_2$	1.25	141.6	62.4	10.3
C_6H_4BrF	0.93	118.1	91.8	10.3
$C_6H_4Br_2$	1.14	136.1	70.5	10.4

Diffusion behaviors for various molecules in AFI zeolite.

To validate the MD simulations that indicated asymmetric rotations slow diffusion in zeolites, several types of experiments were performed to determine molecular diffusion. Firstly, the diffusion behaviors of $C_6H_4F_2$, C_6H_4BrF, and $C_6H_4Br_2$ in SBA-15 (mesoporous silica) and $AlPO_4$-5 (AFI) zeolite were characterized by dynamic breakthrough curves, which could evaluate the transportation properties of molecules through nanoporous materials[65–68]. The X-ray diffraction (XRD) patterns, N_2 adsorption–desorption isotherms, scanning electron microscopy (SEM) images, and pore size distribution for zeolite and mesoporous SBA-15 are shown in Fig. 5A, D, as well as Supplementary Figs. 20–22. The SBA-15 possesses well-ordered mesopores, whereas $AlPO_4$-5 has abundant micropores. Due to the large pore size of SBA-15, the diffusion order of the halogenated benzene is $C_6H_4F_2 > C_6H_4BrF > C_6H_4Br_2$ (Fig. 5B), which gives a breakthrough time of about 11, 15, and 20 min, respectively. This result agrees well with the size of molecules. However, the diffusion order is altered in microporous $AlPO_4$-5 zeolites (Fig. 5E), which follows the order of $C_6H_4F_2 > C_6H_4Br_2 > C_6H_4BrF$, exhibiting the breakthrough time at about 25, 48, and 63 min, respectively. The detailed parameter description for the breakthrough measurements was shown in Methods and the repeatable experiment (Supplementary Methods and Fig. 23) indicated that internal/external diffusion and packing efficiency of adsorbent molecules have no effect on the repetition of breakthrough measurements.

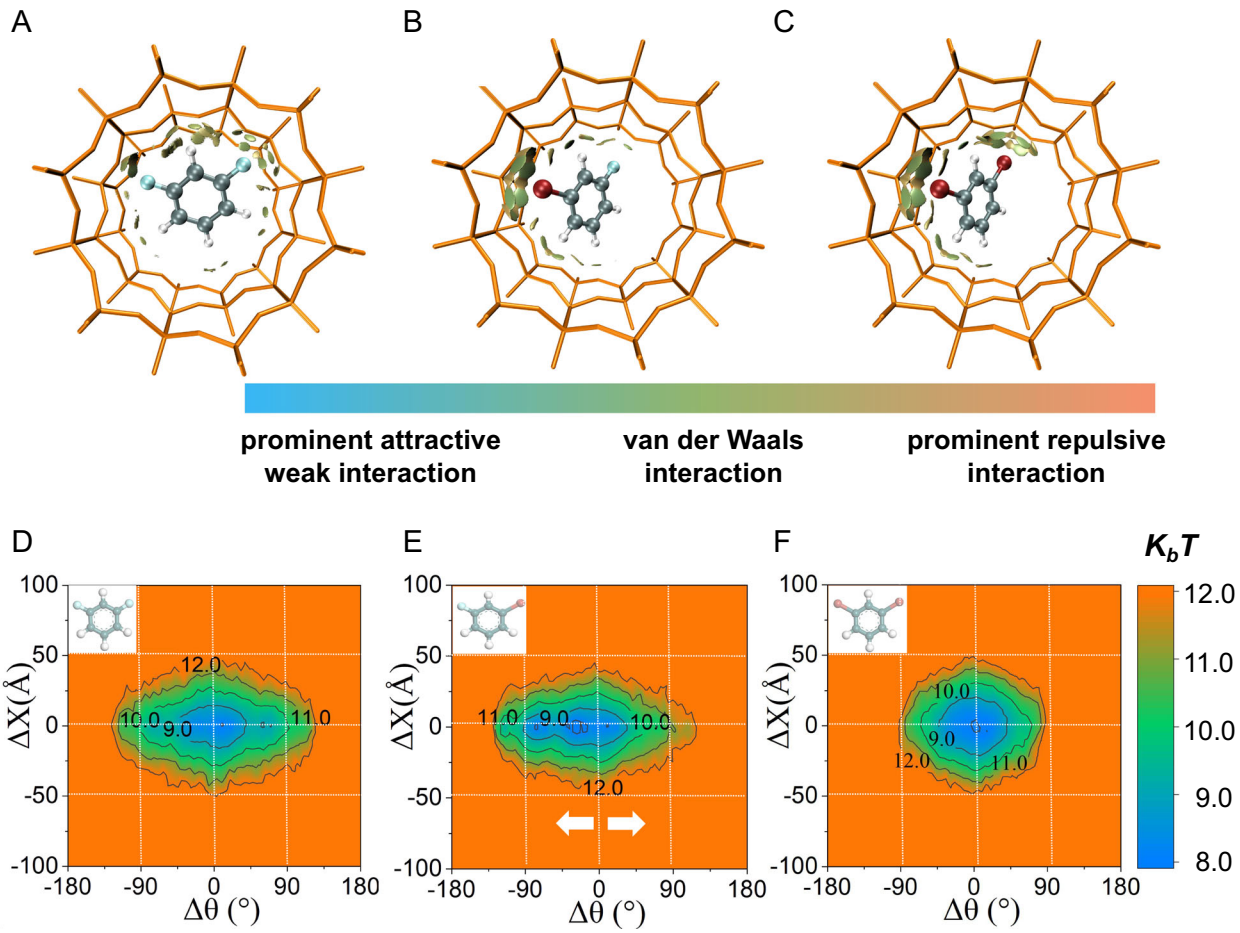

Fig. 3 | Interaction energy and two-dimensional free energy. Isosurface plots of reduced density gradient (isovalue = 0.500 a. u.) for (**A**) $C_6H_4F_2$, (**B**) C_6H_4BrF, and (**C**) $C_6H_4Br_2$ in AFI zeolite. The isosurfaces of reduced density gradient were colored according to the magnitude of sign(λ_2)ρ, and the RGB scale was indicated. The green region represents van der Waals interaction. The dark green, white, cyan and dark red balls represent C, H, F and Br atoms, respectively. Two-dimensional free energy contour plots correlate rotational angle difference (Δθ) and translational displacement (ΔX) for (**D**) $C_6H_4F_2$, (**E**) C_6H_4BrF, and (**F**) $C_6H_4Br_2$ in AFI zeolite, at a time interval of 100 ps. K_b and T are Boltzmann constant and temperature, respectively.

https://doi.org/10.1038/s41467-025-57242-6

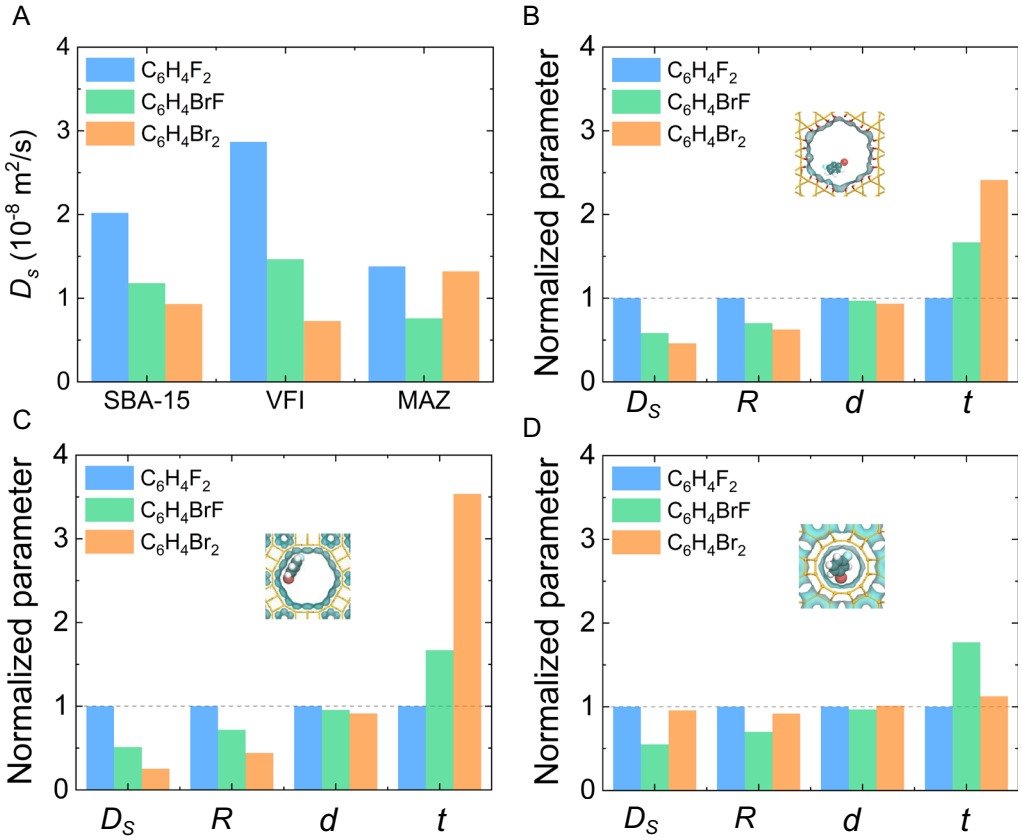

Fig. 4 | Diffusion in other materials. A Self-diffusion coefficient (D_s) for $C_6H_4F_2$, C_6H_4BrF, and $C_6H_4Br_2$ inside SBA-15 model, microporous zeolites with VFI and MAZ topologies at 298 K. Normalized (to $C_6H_4F_2$) D_s, diffusion radius (R), jump length (d), and residence time (t) for $C_6H_4F_2$, C_6H_4BrF, and $C_6H_4Br_2$ in **B** mesoporous SBA-15 model, and microporous zeolites with **C** VFI and **D** MAZ topologies.

Secondly, the uptake rate measurements, which could quantitate the diffusion coefficient in porous materials[69,70], were carried out by an intelligent gravimetric analyzer (IGA). In Fig. 5C, F, the D_{app}/l^2 was used to represent the effective diffusivity normalized by l^2 (l was the half thickness of the characteristic length of crystal). The large D_{app}/l^2 represented the fast diffusion of guest molecules within zeolite crystal. The trends of apparent diffusivity (D_{app} in Fig. 5C, F and Supplementary Fig. 24) in both SBA-15 and $AlPO_4$-5 were in good agreement with the theoretical calculations. Then, highly accurate uptake rates of $C_6H_4F_2$, $C_6H_4Br_2$ and C_6H_4BrF molecules within individual $AlPO_4$-5 (AFI) zeolite crystal (Fig. 5G) at 298 K were measured by synchrotron radiation-based infrared microscope (SR-IRM)[71]. Uptake rate curves of $C_6H_4F_2$, $C_6H_4Br_2$ and C_6H_4BrF molecules at 298 K were shown in Fig. 5H. The diffusivity also follows: $D(C_6H_4F_2) > D(C_6H_4Br_2) > D(C_6H_4BrF)$ (Methods and Supplementary Fig. 25). Furthermore, we also performed QENS to get the self-diffusion coefficient (Methods and Supplementary Fig. 26). The long-range self-diffusivity of the C_6H_4BrF molecule confined in the $AlPO_4$-5 is found to be $2.66 \pm 0.65 \times 10^{-9}$ m^2s^{-1}. This value is of the same order of magnitude as predicted from simulations (1.1×10^{-9} to 9.3×10^{-9} m^2s^{-1}, Supplementary Table 7).

^2H NMR experiments have been widely used for investigating both rotational and translational motions[61–63,72,73]. Recently, we also performed ^2H NMR experiments to investigate the dynamical motion of 1,2,4-trimethyl benzene and acetonitrile inside zeolite[74,75]. In this work, ^2H NMR experiments have been utilized to verify symmetric rotations for $C_6H_4F_2$ and $C_6H_4Br_2$, in contrast to asymmetric rotation for C_6H_4BrF. The details of the ^2H NMR experimental procedures and simulation methods are provided in Methods. As shown in Fig. 5I, the symmetric molecules (i.e. $C_6D_4F_2$ and $C_6D_4Br_2$) present similar Pake doublet spectra, with simulation results aligning closely with the experimental data (Supplementary Fig. 27). This consistency demonstrates that the reorientations for the halogen atoms in $C_6D_4F_2$ and $C_6D_4Br_2$ are equivalent, causing similar ^2H reorientation processes for each ^2H atom within a single molecule. In contrast, the ^2H NMR spectrum for C_6D_4BrF exhibits a distinct lineshape from that of symmetric molecules. Similar pattern can be reproduced by modeling larger-degree reorientation for F atom but smaller-degree reorientation for Br atom, that is asymmetric rotation, which leads to much more varied ^2H reorientations compared to symmetric rotation models (Supplementary ^2H NMR Simulation Methods).

Discussion

In summary, the combined effort of the molecular dynamics simulation, experimental breakthrough curves, uptake measurement by intelligent gravimetric analyzer, as well as SR-IRM, QENS, and ^2H solid-state NMR techniques demonstrated the coupling between rotation and translation during the diffusion process under confinement. In the bulk phase and inside channels with large pore sizes, the diffusivity was determined by the size of molecules and the interaction energy between host and guest. However, since asymmetric rotation significantly slows diffusion, the order of molecular diffusion changes, that is, molecules with larger symmetric shapes may diffuse faster than smaller asymmetric molecules in a tightly confined environment, even if the adsorption energy is stronger. These findings provide fundamental insights into the mechanism of diffusion inside the confined space from both rotation and translation, which could open avenues for catalysis or separation by molecular asymmetry through nanoporous materials.

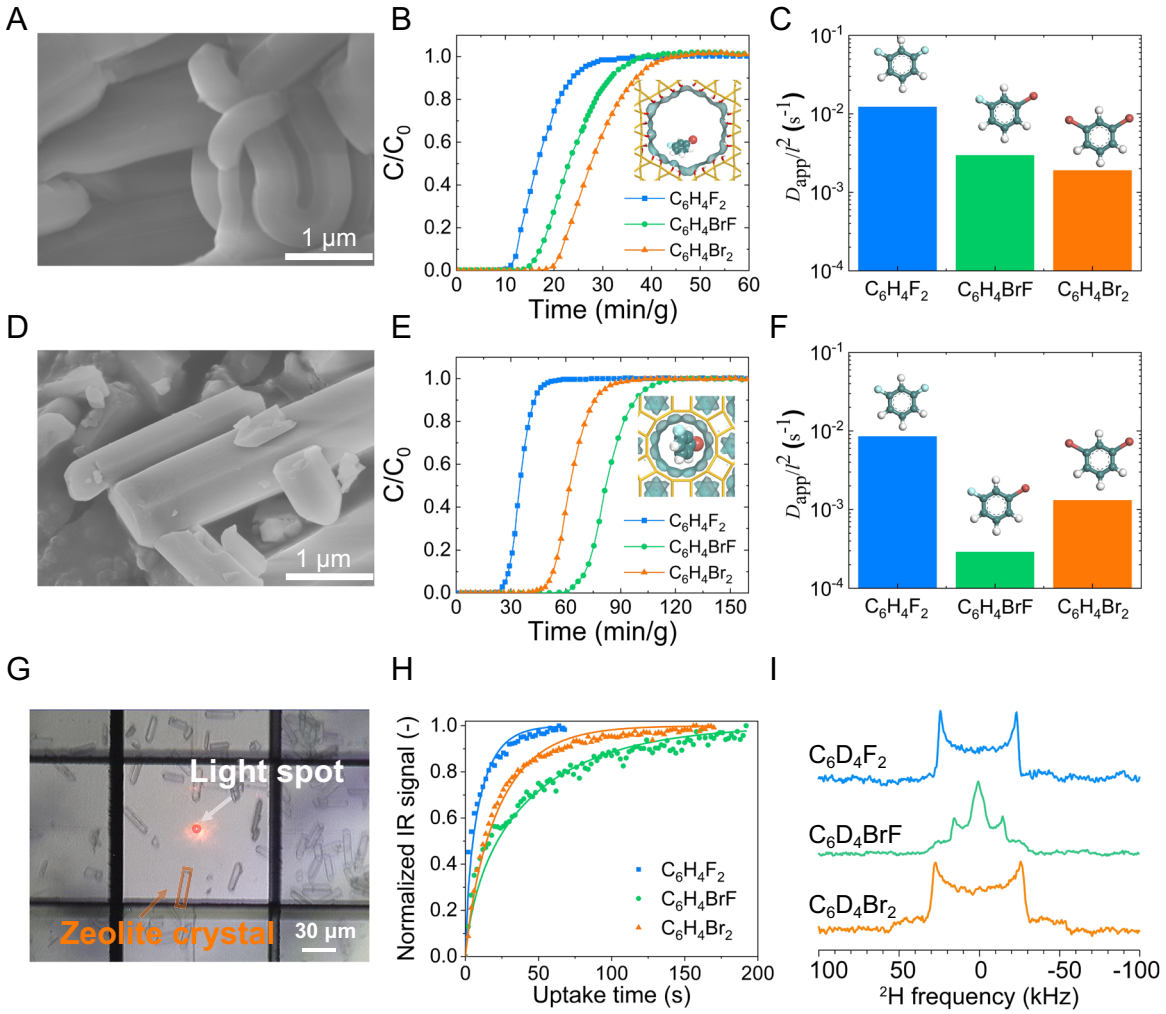

Fig. 5 | Experimental results. A SEM image of SBA-15 (mesoporous silica), **B** breakthrough curves, and **C** apparent diffusivity (D_{app}) of $C_6H_4F_2$, C_6H_4BrF, and $C_6H_4Br_2$ in SBA-15 at 298 K obtained from Intelligent Gravimetric Analyzer (IGA) uptake experiments. The C/C_0 represents the relative concentration of the gas. The dark green, white, cyan and dark red balls represent C, H, F and Br atoms, respectively. **D** SEM image of $AlPO_4$-5 (AFI), **E** breakthrough curves, and **F** D_{app} of $C_6H_4F_2$, C_6H_4BrF, and $C_6H_4Br_2$ in $AlPO_4$-5 at 298 K obtained from IGA uptake experiments. D_{app} is the apparent diffusivity of guest molecules and l is the half thickness of the characteristic length of crystal. Uptake measurements of guest molecules obtained from synchrotron radiation-based infrared microscope (SR-IRM). **G** Optical view of SR-IRM and selected $AlPO_4$-5 zeolite crystal with large size. Light spot is indicated by the visible light. **H** Uptake rate curves of $C_6H_4F_2$, $C_6H_4Br_2$ and C_6H_4BrF molecules at 298 K by SR-IRM. **I** ^2H solid-state NMR spectra of $C_6D_4F_2$, C_6D_4BrF and $C_6D_4Br_2$ in $AlPO_4$−5 at 298 K.

Methods

Molecular dynamics (MD) simulation

The initial framework of MAZ, AFI and VFI was taken from the International Zeolites Associations (IZA) database[51], and the lattice parameters as well as loading number of molecules were shown in Supplementary Table 9. AFI (Supplementary Fig. 4A) and MAZ (Supplementary Fig. 4B) mainly consisted of straight 12-ring channel with a window size of 7.3 × 7.3 Å^2 and 7.4 × 7.4 Å^2 along [001] direction, respectively, while VFI consisted of 18-ring straight channels with pore sizes of 12.7 × 12.7 Å^2 (Supplementary Fig. 4C). In addition, the mesoporous SBA-15 model with the pore size of 20.0 × 20.0 Å^2 has also been built (Supplementary Fig. 4D and Model).

MD simulations were performed in the canonical ensemble (NVT), where the number of particles (N), volume (V), and temperature (T) were kept constant. The simulated temperature was 298 K and controlled by a Nosé-Hoover thermostat with a coupling time constant of 0.1 ps. The leapfrog Verlet algorithm was used to integrate the Newton's equations of motion with a time step of 1.0 fs. Each MD simulation was equilibrated over 1×10^5 steps, and then the following 1×10^7 steps were used to study the diffusion behaviors (e.g. diffusion coefficient and diffusion trajectory) of adsorbate molecules. The COMPASS force field[76–79] was used and the cutoff radius was 12.5 Å. The trajectories were recorded every 1000 steps, and 5–10 independent MD simulations were conducted for better statistics.

A continuous-time random-walk (CTRW) coarse graining method

In coarse-graining time algorithm[28,58,59], the center of the *k-th* dynamic basin of the tagged methane molecule, $\bar{R}(n)_k$, was done iteratively as Eq. (1)

$$\bar{R}(n)_k = \frac{(n-1)\bar{R}(n-1)_k + R(n)}{n} \tag{1}$$

The average was updated until $R\ (n+1)$ walked out of a certain range:

$$\left|R(n+1) - \bar{R}(n)_k\right| \begin{cases} \le D_{max}\ update\ the\ basin\ center\ position \\ > D_{max}\ start\ the\ new\ basin \end{cases} \tag{2}$$

D_{max} was set to 8.5, 8.5, 7.5 and 11.0 Å respectively, which were found to be a reasonable value for the molecules, as a threshold of the

basin crossing in AFI, VFI, MAZ, zeolites and SBA-15 model, respectively. The past n snapshots were defined as a dynamical basin centered at $\bar{R}(n)_k$. If the labeled molecule jumped into a new basin according to Eq. (2), the running index n was updated to 1. The residence time τ was defined as the average waiting time of methane within dynamic basin, while the jump length d was the average distance between two consecutive basin centers $\langle \bar{R}_{k+1} - \bar{R}_k \rangle$.

Mixed gases breakthrough experiment

The breakthrough experiment was carried out on a Micromeritics Autochem 2920 apparatus with mass spectrum (Supplementary Fig. 30). In a repeatable experiment, the tube (6 mm inner diameter × 190 mm) packed with 50 mg of the sample (40-60 mesh) was first purged with He flow (30 mL/min) for 3 h at 150 °C and then cooled to 25 °C. Subsequently, the room-temperature saturated vapor of adsorbed gas (e.g. $C_6H_4F_2$, C_6H_4BrF, and $C_6H_4Br_2$) was introduced by He flow at 20 mL/min. Outlet gas from the tube was monitored by using mass spectrum (Hiden Analytical, HPR-20 R&D) with an ion source-detector. It should be pointed out that all the chemicals were analytical grade and used directly without further purification.

Uptake measurement

The uptake rate measurements were first carried out by use of the Intelligent Gravimetric Analyzer (IGA-100, Hiden Analytical). Especially, in order to enhance the permeability of probe gas or vapor to samples, homemade mesh type of sample cell was used. About 15 mg $AlPO_4$-5 and SBA-15 samples were added to the chamber, and outgassed until a constant weight was achieved at pressure of 10^{-6} mbar and temperature of 623 K for at least 6 h. Then a steam of probe vapor was introduced into the system with a carefully controlling quantity in order to ensure the isobaric and isothermal process. Meanwhile, mass change with buoyancy corrections, system pressure and sample temperature were recorded in real-time. The uptake curves of substituted benzene have been performed in $AlPO_4$-5 and SBA-15 at 298 K (0 → 0.25 mbar).

To get more accurate intracrystalline diffusivity, the uptake rate measurements by synchrotron radiation-based infrared microscope has been performed. The $AlPO_4$-5 zeolites with large crystal size were synthesized by the recipe from reference[80]. The experiments were performed by use of a Fourier transform IR microscope (Bruker Hyperion 3000) composed of a spectrometer (Bruker vertex 80 v) and a 15× optical microscope[81,82]. The in-situ optical reaction cell with BaF_2 window in this device is connected to a saturated vapor system and mounted on a movable platform under the microscope. Such an arrangement facilitates the selection of a reasonably shaped crystallite for subsequent uptake rate measurements. Sample activation was accomplished by heating under air purging at a rate of 10 K/min up to 673 K and kept for 0.5 h, and then the sweeping of nitrogen for 1 h. The total dead-volume of the uptake system (including dead-volume of cell and pipe) is less than 0.5 mL, the flow rate of nitrogen is 40 mL/min, which can avoid the effect of dead-volume on the uptake rate measurements.

Quasi-elastic neutron scattering (QENS)

QENS experiment was performed using the Back-scattering Silicon Spectrometer (BASIS)[83] at the spallation neutron source of the Oak Ridge National Laboratory. QENS spectra were collected by spinning the choppers at 60 Hz and selecting the bandwidth of incident neutron centered at 6.4 Å. This configuration of the instrument covers an energy transfer range of ±100 μeV and Q range of 0.2 $Å^{-1}$–2 $Å^{-1}$, providing an energy resolution of ~3.4 μeV (Q-averaged full width at half maximum). The sample was placed in an aluminum foil and made a pouch, rolled, and put into an annular aluminum can inside a glove box. The sample was sealed with an indium ring. The sample temperature was controlled using a close cycle refrigerator (CCR). QENS data was collected at 298 K, and the sample specific resolution was measured at 5 K. The data was reduced and analyzed using Mantid[84] and DAVE[85] software, respectively.

^{2}H NMR experiments

Prior to adsorb deuterated 1,3-halogen-substituted benzene-d_4, AlPO-5 zeolites were dehydrated at 693 K and <10^{-3} Pa for 10 h, weighed and then transferred into rotors within an Ar-filled glovebox. Specified volumes of 1,3-halogen-substituted benzene-d_4 were introduced into the rotors using microsyringe, followed by sealing the rotor caps. $C_6D_4F_2$ was introduced as a CH_2Cl_2 solution at a concentration of 0.07 g/mL, with a loading for $C_6D_4F_2/CH_2Cl_2$ solution of 99 μL/$g_{zeolite}$. $C_6D_4Br_2$ and C_6D_4BrF were used as pure compounds with loading of 11 μL/$g_{zeolite}$ and 12 μL/$g_{zeolite}$, respectively. The $C_6D_4F_2$-loaded sample was equilibrated at room temperature overnight, while the $C_6D_4Br_2$ and C_6D_4BrF loaded samples were equilibrated at 383 K for 2 h. Before performing ^{2}H NMR experiments, the samples were evacuated at room temperature for 3 min to remove CH_2Cl_2 and other loosely-bound molecules.

Static ^{2}H NMR experiments were measured at room temperature on a Bruker Avance NEO 400 spectrometer (9.4 T) with a 4 mm HXY MAS NMR probe. The spectra were recorded using the quadrupolar echo (QE) method with a π/2 pulse of 3.5 μs, an echo delay of 35 μs, and a recycle delay of 2 s. 31320 scans were accumulated for each ^{2}H NMR spectrum.

Data availability

The main data generated in this study are provided in the Supplementary Information, other data presented in this manuscript are available from the corresponding authors upon request. Source data are provided with this paper.

Code availability

The code used in this manuscript is available from the corresponding authors upon request.

References

1. Bunde, A., Caro, J., Karger, J. & Vogl, G. *Diffusive Spreading in Nature, Technology and Society* (Springer, 2007).
2. Karger, J. & Ruthven, D. M. Diffusion in Nanoporous Materials: Fundamental Principles, Insights and Challenges. *N. J. Chem.* **40**, 4027–4048 (2016).
3. Karger, J., Ruthven, D. M. & Valiullin, R. Diffusion in Nanopores: Inspecting the Grounds. *Adsorption* **27**, 267–281 (2021).
4. Chmelik, C., Heinke, L., Valiullin, R. & Karger, J. A New View of Diffusion in Nanoporous Materials. *Chem. Ing. Tech.* **82**, 779–804 (2010).
5. Yuan, J. M. et al. Hyperloop-Like Diffusion of Long-Chain Molecules under Confinement. *Nat. Commun.* **14**, 1735 (2023).
6. Smit, B. & Maesen, T. L. M. Molecular Simulations of Zeolites: Adsorption, Diffusion, and Shape Selectivity. *Chem. Rev.* **108**, 4125–4184 (2008).
7. Hahn, K., Karger, J. & Kukla, V. Single-File Diffusion Observation. *Phys. Rev. Lett.* **76**, 2762–2765 (1996).
8. Wei, Q. H., Bechinger, C. & Leiderer, P. Single-File Diffusion of Colloids in One-Dimensional Channels. *Science* **287**, 625–627 (2000).
9. Tsekov, R. & Smirniotis, P. G. Resonant Diffusion of Normal Alkanes in Zeolites: Effect of the Zeolite Structure and Alkane Molecule Vibrations. *J. Phys. Chem. B* **102**, 9385–9391 (1998).
10. Ruckenstein, E. & Lee, P. S. Resonant Diffusion. *Phys. Lett. A* **56**, 423–424 (1976).
11. Runnebaum, R. C. & Maginn, E. J. Molecular Dynamics Simulations of Alkanes in the Zeolite Silicalite: Evidence for Resonant Diffusion Effects. *J. Phys. Chem. B* **101**, 6394–6408 (1997).

12. Yuan, J. M. et al. Thermal Resistance Effect on Anomalous Diffusion of Molecules under Confinement. *Proc. Natl. Acad. Sci. USA* **118**, e2102097118 (2021).
13. Kolokathis, P. D., Kali, G., Jobic, H. & Theodorou, D. N. Diffusion of Aromatics in Silicalite-1: Experimental and Theoretical Evidence of Entropic Barriers. *J. Phys. Chem. C* **120**, 21410–21426 (2016).
14. Derouane, E. G., Andre, J. M. & Lucas, A. A. Surface Curvature Effects in Physisorption and Catalysis by Microporous Solids and Molecular-Sieves. *J. Catal.* **110**, 58–73 (1988).
15. Yashonath, S. & Ghorai, P. K. Diffusion in Nanoporous Phases: Size Dependence and Levitation Effect. *J. Phys. Chem. B* **112**, 665–686 (2008).
16. Borah, B. J., Jobic, H. & Yashonath, S. Levitation Effect in Zeolites: Quasielastic Neutron Scattering and Molecular Dynamics Study of Pentane Isomers in Zeolite NaY. *J. Chem. Phys.* **132**, 144507 (2010).
17. Nag, S., Ananthakrishna, G., Maiti, P. K. & Yashonath, S. Separating Hydrocarbon Mixtures by Driving the Components in Opposite Directions: High Degree of Separation Factor and Energy Efficiency. *Phys. Rev. Lett.* **124**, 255901 (2020).
18. Bhide, S. Y. & Yashonath, S. N-Pentane and Isopentane in One-Dimensional Channels. *J. Am. Chem. Soc.* **125**, 7425–7434 (2003).
19. Ghorai, P. K., Yashonath, S., Demontis, P. & Suffritti, G. B. Diffusion Anomaly as a Function of Molecular Length of Linear Molecules: Levitation Effect. *J. Am. Chem. Soc.* **125**, 7116–7123 (2003).
20. Dubbeldam, D., Calero, S., Maesen, T. L. M. & Smit, B. Incommensurate Diffusion in Confined Systems. *Phys. Rev. Lett.* **90**, 245901 (2003).
21. Gorring, R. L. Diffusion of Normal Paraffins in Zeolite-T - Occurrence of Window Effect. *J. Catal.* **31**, 13–26 (1973).
22. Dubbeldam, D., Calero, S., Maesen, T. L. M. & Smit, B. Understanding the Window Effect in Zeolite Catalysis. *Angew. Chem. Int. Ed.* **42**, 3624–3626 (2003).
23. Zhao, J. H. et al. Nitrogen Rejection from Methane Via a "Trapdoor" K-ZSM-25 Zeolite. *J. Am. Chem. Soc.* **143**, 15195–15204 (2021).
24. Coudert, F. X. & Kohen, D. Molecular Insight into CO2 "Trapdoor" Adsorption in Zeolite Na-RHO. *Chem. Mater.* **29**, 2724–2730 (2017).
25. Shang, J. et al. Discriminative Separation of Gases by a "Molecular Trapdoor" Mechanism in Chabazite Zeolites. *J. Am. Chem. Soc.* **134**, 19246–19253 (2012).
26. Wang, X. H. et al. The Inorganic Cation-Tailored "Trapdoor" Effect of Silicoaluminophosphate Zeolite for Highly Selective CO2 Separation. *Chem. Sci.* **12**, 8803–8810 (2021).
27. Cnudde, P. et al. Light Olefin Diffusion During the MTO Process on H-SAPO-34: A Complex Interplay of Molecular Factors. *J. Am. Chem. Soc.* **142**, 6007–6017 (2020).
28. Gao, S. et al. Cavity-Controlled Diffusion in 8-Membered Ring Molecular Sieve Catalysts for Shape Selective Strategy. *J. Catal.* **377**, 51–62 (2019).
29. Gao, M. B., Li, H., Ye, M. & Liu, Z. M. An Approach for Predicting Intracrystalline Diffusivities and Adsorption Entropies in Nanoporous Crystalline Materials. *AIChE J.* **66**, e16991 (2020).
30. Liu, Z. Q. et al. Dependence of Zeolite Topology on Alkane Diffusion inside Diverse Channels. *AIChE J.* **66**, e16269 (2020).
31. Liu, Z. Q. et al. Synergistically Enhance Confined Diffusion by Continuum Intersecting Channels in Zeolites. *Sci. Adv.* **7**, eabf0775 (2021).
32. Beerdsen, E., Dubbeldam, D. & Smit, B. Molecular Understanding of Diffusion in Confinement. *Phys. Rev. Lett.* **95**, 164505 (2005).
33. Jobic, H. Diffusion of Linear and Branched Alkanes in ZSM-5. A Quasi-Elastic Neutron Scattering Study. *J. Mol. Catal. A Chem.* **158**, 135–142 (2000).
34. van Baten, J. M. & Krishna, R. Entropy Effects in Adsorption and Diffusion of Alkane Isomers in Mordenite: An Investigation Using CBMC and MD Simulations. *Microporous Mesoporous Mater.* **84**, 179–191 (2005).
35. Schuring, D., Koriabkina, A. O., de Jong, A. M., Smit, B. & van Santen, R. A. Adsorption and Diffusion of N-Hexane/2-Methylpentane Mixtures in Zeolite Silicalite: Experiments and Modeling. *J. Phys. Chem. B* **105**, 7690–7698 (2001).
36. Verploegh, R. J. et al. Screening Diffusion of Small Molecules in Flexible Zeolitic Imidazolate Frameworks Using a DFT-Parameterized Force Field. *J. Phys. Chem. C.* **123**, 9153–9167 (2019).
37. DeLuca, M. & Hibbitts, D. Predicting Diffusion Barriers and Diffusivities of C6–C12 Methylbenzenes in MFI Zeolites. *Microporous Mesoporous Mater.* **333**, 111705 (2022).
38. Wang, C. et al. Importance of Zeolite Wettability for Selective Hydrogenation of Furfural over Pd@Zeolite Catalysts. *ACS Catal.* **8**, 474–481 (2017).
39. Matsubara, H., Pichierri, F. & Kurihara, K. Mechanism of Diffusion Slowdown in Confined Liquids. *Phys. Rev. Lett.* **109**, 197801 (2012).
40. Kojic-Prodic, B. & Stefanic, Z. Symmetry Versus Asymmetry in the Molecules of Life: Homomeric Protein Assemblies. *Symmetry* **2**, 884–906 (2010).
41. Zhou, S. et al. Asymmetric Pore Windows in MOF Membranes for Natural Gas Valorization. *Nature* **606**, 706–712 (2022).
42. Sharma, M. & Yashonath, S. Levitation Effect: Role of Symmetry and Dependence of Diffusivity on the Bond Length of Homonuclear and Heteronuclear Diatomic Species. *J. Phys. Chem. B* **115**, 3514–3521 (2011).
43. Shaw, R. S., Packard, N., Schröter, M. & Swinney, H. L. Geometry-Induced Asymmetric Diffusion. *Proc. Natl. Acad. Sci. USA* **104**, 9580 (2007).
44. Kolomeisky, A. B. Channel-Facilitated Molecular Transport across Membranes: Attraction, Repulsion, and Asymmetry. *Phys. Rev. Lett.* **98**, 048105 (2007).
45. Dhiman, I., Bhowmik, D., Shrestha, U. R., Cole, D. R. & Gautam, S. Effect of Molecular Shape on Rotation under Severe Confinement. *Chem. Eng. Sci.* **180**, 33–41 (2018).
46. Dhiman, I., Shrestha, U. R., Bhowmik, D., Cole, D. R. & Gautam, S. Influence of Molecular Shape on Self-Diffusion under Severe Confinement: A Molecular Dynamics Study. *Chem. Phys.* **516**, 92–102 (2019).
47. Alvarez-Ramirez, J., Dagdug, L. & Meraz, M. Asymmetric Diffusion in Heterogeneous Media. *Phys. A* **395**, 193 (2014).
48. Fragiadakis, D. & Roland, C. M. Rotational Dynamics of Simple Asymmetric Molecules. *Phys. Rev. E* **91**, 022310 (2015).
49. Banerjee, P., Yashonath, S. & Bagchi, B. Rotation Driven Translational Diffusion of Polyatomic Ions in Water: A Novel Mechanism for Breakdown of Stokes-Einstein Relation. *J. Chem. Phys.* **146**, 164502 (2017).
50. Chai, Y. C., Dai, W. L., Wu, G. J., Guan, N. J. & Li, L. D. Confinement in a Zeolite and Zeolite Catalysis. *Acc. Chem. Res.* **54**, 2894–2904 (2021).
51. Baerlocher, C., McCusker, L. B. Database of Zeolite Structures. http://www.iza-structure.org/databases/ (2016).
52. Sastre, G. & Corma, A. The Confinement Effect in Zeolites. *J. Mol. Catal. A Chem.* **305**, 3–7 (2009).
53. Toda, J. & Sastre, G. Diffusion of Trimethylbenzenes, Toluene, and Xylenes in UWY Zeolite as a Catalyst for Transalkylation of Trimethylbenzenes with Toluene. *J. Phys. Chem. C.* **122**, 7885–7897 (2018).
54. Liu, Z. et al. Roles of 8-Ring and 12-Ring Channels in Mordenite for Carbonylation Reaction: From the Perspective of Molecular Adsorption and Diffusion. *J. Catal.* **369**, 335–344 (2019).
55. Weeks, E. R., Crocker, J. C., Levitt, A. C., Schofield, A. & Weitz, D. A. Three-Dimensional Direct Imaging of Structural Relaxation near the Colloidal Glass Transition. *Science* **287**, 627–631 (2000).
56. Zhang, Z. T., Zhao, X. & Cao, B. Y. Diffusion Tensors of Arbitrary-Shaped Nanoparticles in Fluid by Molecular Dynamics Simulation. *Sci. Rep.* **9**, 18943 (2019).

57. Araque, J. C., Daly, R. P. & Margulis, C. J. A Link between Structure, Diffusion and Rotations of Hydrogen Bonding Tracers in Ionic Liquids. *J. Chem. Phys.* **144**, 204504 (2016).
58. Zhang, Q., Wu, T. M., Chen, C., Mukamel, S. & Zhuang, W. Molecular Mechanism of Water Reorientational Slowing Down in Concentrated Ionic Solutions. *Proc. Natl. Acad. Sci. USA* **114**, 10023–10028 (2017).
59. Qvist, J., Schober, H. & Halle, B. Structural Dynamics of Supercooled Water from Quasielastic Neutron Scattering and Molecular Simulations. *J. Chem. Phys.* **134**, 144508 (2011).
60. Zhao, C. et al. Gating Control Effect Facilitates Excellent Gas Selectivity in a Novel Na-SSZ-27 Zeolite. *Chem. Commun.* **57**, 4170–4173 (2021).
61. Kolokolov, D. I. et al. Uncovering the Rotation and Translational Mobility of Benzene Confined in UiO-66 (Zr) Metal–Organic Framework by the 2H NMR–QENS Experimental Toolbox. *J. Phys. Chem. C* **121**, 2844–2857 (2017).
62. Khudozhitkov, A. E., Arzumanov, S. S., Kolokolov, D. I. & Stepanov, A. G. Dynamics of Xylene Isomers in MIL-53 (Al) MOF Probed by Solid State 2H NMR. *Microporous Mesoporous Mater.* **300**, 110155 (2020).
63. Kolokolov, D. I. et al. Rotational and Translational Motion of Benzene in ZIF-8 Studied by 2H NMR: Estimation of Microscopic Self-Diffusivity and Its Comparison with Macroscopic Measurements. *J. Phys. Chem. C* **118**, 12873–12879 (2014).
64. Krishna, R. & van Baten, J. M. A Molecular Dynamics Investigation of a Variety of Influences of Temperature on Diffusion in Zeolites. *Microporous Mesoporous Mater.* **125**, 126–134 (2009).
65. Zhu, H. Y. et al. Constructing Hierarchical Interfaces: TiO2-Supported PtFe-FeOx Nanowires for Room Temperature CO Oxidation. *J. Am. Chem. Soc.* **137**, 10156–10159 (2015).
66. Chen, F. Q. et al. Deep Desulfurization with Record SO2 Adsorption on the Metal-Organic Frameworks. *J. Am. Chem. Soc.* **143**, 9040–9047 (2021).
67. Kan, X. et al. Sulfonated and Ordered Mesoporous Polymers for Reversible Adsorption of Ammonia: Elucidation of Sequential Pore-Space Diffusion. *Chem. Eng. J.* **451**, 139085 (2023).
68. Cui, X. L. et al. Pore Chemistry and Size Control in Hybrid Porous Materials for Acetylene Capture from Ethylene. *Science* **353**, 141–144 (2016).
69. Lee, L. K. & Ruthven, D. M. Analysis of Thermal Effects in Adsorption Rate Measurements. *J. Chem. Soc. Faraday Trans. I* **75**, 2406–2422 (1979).
70. Karger, J. & Ruthven, D. M. Diffusion in Zeolites - Comparison of Sorption and Nuclear Magnetic-Resonance Diffusivities. *J. Chem. Soc. Faraday Trans. I* **77**, 1485–1496 (1981).
71. Qian, Q. et al. Single-Particle Spectroscopy on Large SAPO-34 Crystals at Work: Methanol-to-Olefin versus Ethanol-to-Olefin Processes. *Chem. Eur. J.* **19**, 11204–11215 (2013).
72. Vold, R. L. & Hoatson, G. L. Effects of Jump Dynamics on Solid State Nuclear Magnetic Resonance Line Shapes and Spin Relaxation Times. *J. Magn. Reason.* **198**, 57–72 (2009).
73. Steigel, A. & Spiess, H. W. Rotation of Molecules and Nuclear Spin Relaxation. In: *Dynamic NMR Spectroscopy. NMR Basic Principles and Progress* (Springer, 1978).
74. Ji, Y. et al. Untangling Framework Confinements: A Dynamical Study on Bulky Aromatic Molecules in MFI Zeolites. *ACS Catal.* **12**, 15288–15297 (2022).
75. Gong, K. et al. Acidity and Local Confinement Effect in Mordenite Probed by Solid-State NMR Spectroscopy. *J. Phys. Chem. Lett.* **12**, 2413–2422 (2021).
76. Sun, H. Compass: An Ab Initio Force-Field Optimized for Condensed-Phase Applications - Overview with Details on Alkane and Benzene Compounds. *J. Phys. Chem. B* **102**, 7338–7364 (1998).
77. Wu, J. Y., Liu, Q. L., Xiong, Y., Zhu, A. M. & Chen, Y. Molecular Simulation of Water/Alcohol Mixtures' Adsorption and Diffusion in Zeolite 4A Membranes. *J. Phys. Chem. B* **113**, 4267–4274 (2009).
78. Ari, M. U., Ahunbay, M. G., Yurtsever, M. & Erdem-Senatalar, A. Molecular Dynamics Simulation of Water Diffusion in MFI-Type Zeolites. *J. Phys. Chem. B* **113**, 8073–8079 (2009).
79. Deore, S., Simoncic, P. & Navrotsky, A. Molecular Mechanics Studies of Thionin Blue in Zeolite Mordenite. *Microporous Mesoporous Mater.* **109**, 342–349 (2008).
80. Liu, J. et al. Carbon Dots in Zeolites: A New Class of Thermally Activated Delayed Fluorescence Materials with Ultralong Lifetimes. *Sci. Adv.* **3**, e1603171 (2017).
81. Kärger, J. et al. Microimaging of Transient Guest Profiles to Monitor Mass Transfer in Nanoporous Materials. *Nat. Mater.* **13**, 333–343 (2014).
82. Chmelik, C. & Kärger, J. In situ study on molecular diffusion phenomena in nanoporous catalytic solids. *Chem. Soc. Rev.* **39**, 4864–4884 (2010).
83. Mamontov, E. & Herwig, K. W. A Time-of-Flight Backscattering Spectrometer at the Spallation Neutron Source, BASIS. *Rev. Sci. Instrum.* **82**, 085109 (2011).
84. Arnold, O. et al. Mantid—Data Analysis and Visualization Package for Neutron Scattering and μSR Experiments. *Nucl. Instrum. Methods Phys. Res. Sect. A* **764**, 156–166 (2014).
85. Azuah, R. T. et al. DAVE: A Comprehensive Software Suite for the Reduction, Visualization, and Analysis of Low Energy Neutron Spectroscopic Data. *J. Res. Natl. Inst. Stand. Technol.* **114**, 341–358 (2009).

Acknowledgements

This work was supported by the National Key R&D Program of China (No. 2022YFE0116000 and 2021YFA1502600), the National Science Foundation of China (No. 22125304, 22202215, 22032005, 22241801, 22293021, 22208337, 22002174, 22022804, 22378064, 22325405, 22432005, and U24A20528), the Natural Science Foundation of Hubei Province (2024AFA054), the Postdoctoral Fellowship Program of CPSF under Grant Number GZB20240764, and the Fundamental Research Funds for the Central Universities (20720240060). Numerical calculation is supported by High-Performance Computing Center of Wuhan University of Science and Technology. A portion of this research used resources at the Spallation Neutron Source, a DOE Office of Science User Facility operated by the Oak Ridge National Laboratory. The beam time was allocated to BASIS on proposal number IPTS-34773. We thank the staffs from the BL06B1 beamline of National Facility at Shanghai Synchrotron Radiation Facility for assistance in data collection of infrared spectroscopy.

Author contributions

Z.L. and A.Z. designed the research; Z.L. carried out the theoretical calculations, collated and analyzed the data, and wrote the paper; X.K. and F.J.L. performed breakthrough experiment; M.G. and M.Y. performed the uptake measurement; Y.J., H.L., P.G., and G.H. performed ^{2}H NMR experiments**;** F.Y. and S.X. performed PFG-NMR experiments; J.T. carried out DFT calculation; M.G., F.Q.L., J.X., Q.C., and Y.Z. performed the zeolites preparation and characterization; J.T., J.Y., X.T., and Y.L. provided helpful discussion; N.O., N.J., and C.L. performed QENS experiment; Z.L, A.Z., G.H., M.Y., and F.J.L. supervised the work and revised the article. All authors discussed the results and commented on the manuscript.

Competing interests

The authors declare no competing interests.

Additional information

Supplementary information The online version contains supplementary material available at https://doi.org/10.1038/s41467-025-57242-6.

Correspondence and requests for materials should be addressed to Zhiqiang Liu, Guangjin Hou, Mao Ye, Fujian Liu or Anmin Zheng.

Peer review information *Nature Communications* thanks Daniil Kolokolov and the other, anonymous, reviewer(s) for their contribution to the peer review of this work. A peer review file is available.

Reprints and permissions information is available at http://www.nature.com/reprints

Publisher's note Springer Nature remains neutral with regard to jurisdictional claims in published maps and institutional affiliations.

Open Access This article is licensed under a Creative Commons Attribution-NonCommercial-NoDerivatives 4.0 International License, which permits any non-commercial use, sharing, distribution and reproduction in any medium or format, as long as you give appropriate credit to the original author(s) and the source, provide a link to the Creative Commons licence, and indicate if you modified the licensed material. You do not have permission under this licence to share adapted material derived from this article or parts of it. The images or other third party material in this article are included in the article's Creative Commons licence, unless indicated otherwise in a credit line to the material. If material is not included in the article's Creative Commons licence and your intended use is not permitted by statutory regulation or exceeds the permitted use, you will need to obtain permission directly from the copyright holder. To view a copy of this licence, visit http://creativecommons.org/licenses/by-nc-nd/4.0/.

© The Author(s) 2025